Available online at www.sciencedirect.com
ScienceDirect
Trans. Nonferrous Met. Soc. China 32(2022) 721−738
Transactions of Nonferrous Metals Society of China
www.tnmsc.cn

Effects of Mg content on microstructure and mechanical properties of low Zn-containing Al−*x*Mg−3Zn−1Cu cast alloys

Chuan LEI, Qu-dong WANG, Hua-ping TANG, Tian-wen LIU, Zhong-yang LI, Hai-yan JIANG, Kui WANG, Wen-jiang DING

National Engineering Research Center of Light Alloy Net Forming and State Key Laboratory of Metal Matrix Composites, School of Materials Science and Engineering, Shanghai Jiao Tong University, Shanghai 200240, China

Received 7 April 2021; accepted 25 November 2021

Abstract: Effects of Mg content on the microstructure and mechanical properties of low Zn-containing Al−*x*Mg−3Zn−1Cu cast alloys (*x*=3−5, wt.%) were investigated. As Mg content increased in the as-cast alloys, the grains were refined due to enhanced growth restriction, and the formation of η-Mg(AlZnCu)$_2$ and *S*-Al$_2$CuMg phases was inhibited while the formation of *T*-Mg$_{32}$(AlZnCu)$_{49}$ phase was promoted when Mg content exceeded 4 wt.%. The increase of Mg content encumbered the solution kinetics by increasing the size of eutectic phase but accelerated and enhanced the age-hardening through expediting precipitation kinetics and elevating the number density of the precipitates. As Mg content increased, the yield strength and tensile strength of the as-cast, solution-treated and peak-aged alloys were severally improved, while the elongation of the alloys decreased. The tensile strength and elongation of the peak-aged Al−5Mg−3Zn−1Cu alloy exceed 500 MPa and 5%, respectively. Precipitation strengthening implemented by *T*′ precipitates is the predominant strengthening mechanism in the peak-aged alloys and is enhanced by increasing Mg content.

Key words: Mg content; low Zn-containing Al−*x*Mg−3Zn−1Cu cast alloys; microstructure; aging response; strengthening mechanism

1 Introduction

High-strength Al−Mg−Zn−Cu cast alloys are extensively utilized in the automotive and aviation industries [1−4], but these alloys often suffer from poor ductility [1,5,6]. To achieve strength−ductility synergy, composition optimization is often adopted [7,8], and it is usually implemented by adjusting the content and proportion of alloying elements [1,9]. In addition to conventional low Mg-containing Al−Mg−Zn−Cu alloys with high Zn content, many high Mg-containing Al−Mg−Zn−Cu alloys with low Zn content were developed in recent years [10,11] and these alloys were proven to own a favorable combination of strength and ductility [11,12]. Nevertheless, research on these high Mg-containing Al−Mg−Zn−Cu alloys remains inadequate (for instance, composition optimization). Mg is one of the core elements in Al−Mg−Zn−Cu system, and clarifying its effect on the microstructure and mechanical properties is the prerequisite for developing castings.

Al−Zn−Mg−Cu alloys with low or high Mg contents may exhibit distinct microstructure and mechanical behaviors, which has been sufficiently demonstrated in extensive studies [7,13]. Some of these studies are focused on the phase components of the as-cast alloys. The combinations of multiple eutectic phases (including hexagonal η-MgZn$_2$ [14],

Corresponding author: Qu-dong WANG, Tel: +86-21-54742715, E-mail: wangqudong@sjtu.edu.cn
DOI: 10.1016/S1003-6326(22)65828-X

body-centered cubic or icosahedral T-$Mg_{32}(AlZn)_{49}$ [15,16], orthorhombic S-Al_2CuMg [17] and tetragonal θ-Al_2Cu [17] phases) in Al−Mg−Zn−Cu alloys were thought to be affected by Mg content [11,13,14,18]. The dominant eutectic phase is changed from η-$MgZn_2$ for low Mg-containing Al−Mg−Zn−Cu alloys [14,18] to T-$Mg_{32}(AlZn)_{49}$ phase for high Mg-containing alloys [11,13], and the existence of S-Al_2CuMg and θ-Al_2Cu phase in as-cast Al−Mg−Zn−Cu alloys is also related to Mg content [19−21]. Universally, the content of the eutectic phase increases with increasing Mg content [1], and the change of the composition and content of the eutectic phase directly affects the subsequent solid solution process [14,21]. Despite the extensive literature, phase identification is still necessary for specific alloys due to the complexity of the Al−Mg−Zn−Cu system.

It is widely accepted that the strength of Al−Mg−Zn−Cu alloys is improved by increasing Mg content [2,7,9,22], and the strength increment induced by increasing Mg addition is mainly attributed to the enhancement of precipitation strengthening [2,9]. Nevertheless, the precipitation behavior is discrepant in different alloys [10,23−26]. The precipitation sequence in most low Mg-containing Al−Mg−Zn−Cu alloys has been widely accepted as super-saturated solid solution (SSSS) → GP zones (GP I and II) → η' → η [24,26,27]. The GP zones here refer to the internal ordering of Zn and Al/Mg on $\{001\}_{Al}$ planes (GP I) or Zn-rich layers on $\{111\}_{Al}$ planes (GP II) [24,27]. The plate-like metastable η' precipitates formed on $\{111\}_{Al}$ plane are generally responsible for the strength of the peak-aged alloys [24,27]. Studies showed that increasing Mg content can promote the formation of GP I zones [7], improve the volume fraction and reduce the sizes of η' precipitates [7], elevate the precipitation temperature and extend the stable temperature range of η' precipitates [28]. By contrast, the precipitation sequence was modified to SSSS → GP I zones → GP II (T'') → T' → T in the high Mg-containing Al−Mg−Zn−Cu alloys [25,29]. The GP zones here are Zn−Mg clusters without a distinctive structure while T'' precipitates are slightly coarser GP zones with a distinctive structure [25]. The metastable T' precipitates are regarded as the dominant precipitates in peak-aged high Mg-containing Al−Mg−Zn−Cu alloys [30,31], although they were often neglected for their weaker strengthening capacity than η' precipitates [25]. Given the strong pertinence between mechanical properties and precipitates, it is necessary to investigate the effect of Mg content on the precipitation behavior and the strengthening mechanism of these high Mg-containing Al−Mg−Zn−Cu alloys.

Considering the necessity of a systematic evaluation of the effect of Mg content on the microstructure and mechanical properties of high Mg-containing Al−Mg−Zn−Cu alloys with low Zn content, the effects of Mg content on the microstructure, heat treatment, and mechanical properties of Al−xMg−3Zn−1Cu alloys (x=3−5, wt.%) prepared by permanent mold gravity casting were investigated in this work.

2 Experimental

Commercially-pure Al (99.7 wt.%), pure Mg (99.8 wt.%), pure Zn (99.7 wt.%), and Al−50wt.%Cu master alloys were utilized to prepare the studied alloys. The raw materials were melted in an electric resistance furnace at 720 °C. The melt was degassed with 0.3 wt.% C_2Cl_6 powder, and 0.5 wt.% Al−5Ti−B master alloy was added for grain refinement. The ingots with the geometry shown in Fig. 1(a) were fabricated by pouring the melt into a preheated permanent mold (100 °C). The chemical compositions of the alloys were

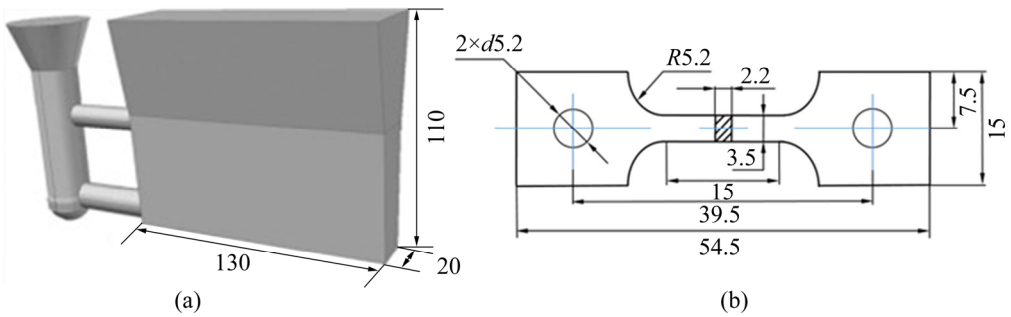

Fig. 1 Sketches of ingots (a) and tensile test specimens (b) (unit: mm)

determined by inductively coupled plasma-atomic emission spectroscopy (ICP-AES, iCAP6300) and are listed in Table 1. The samples were solution treated at 470 °C for various durations ranging from 0.25 to 36 h and water quenched, the as-quenched alloys were stabilized at room temperature for 3 days before aging at 120, 150 and 175 °C for various durations, respectively.

Table 1 Chemical composition of Al−*x*Mg−3Zn−1Cu alloys (wt.%)

x	Mg	Zn	Cu	Ti	B	Fe	Si	Al
3	3.062	3.103	0.971	0.037	0.006	0.272	0.206	Bal.
4	3.914	3.109	0.993	0.024	0.006	0.243	0.194	Bal.
4.5	4.441	3.033	0.951	0.037	0.006	0.207	0.251	Bal.
5	5.116	3.124	1.026	0.027	0.006	0.204	0.211	Bal.

The phase constitutions were determined by an X-ray diffractometer (XRD, Ultima IV) between 2θ=15° and 90° with a scanning rate of 5 (°)/min, and synchronous thermal analysis (STA, STA 449 F3) was conducted between room temperature and 700 °C with a heating rate of 10 °C/min. Samples for microstructure observation were mechanically ground, polished with MgO suspension, and etched with Keller's reagent (5 mL HNO_3, 3 mL HCl, 2 mL HF and 190 mL distilled water) for metallographic observation (OM, Axio Observer A1). Image Pro-Plus software was used for statistical analysis of the grain size, the fraction and size of eutectic phase, and 5 micrographs were inspected for each alloy. The size of eutectic phase is defined as the maximum width of the eutectic phase envelope. The polished samples were also observed by a scanning electron microscope (SEM, Phenom XL), and the compositions of the eutectic phases were determined by X-ray energy dispersive spectroscopy (EDS, Phenom XL). Wafers for transmission electron microscope (TEM) analysis were mechanically ground to about 100 μm thick and twin-jet electropolished in a 30 vol.% nitric-methanol solution at −25 °C. TEM analysis was performed on an FEI Talos F200X transmission electron microscope operating at 200 kV.

Hardness tests were performed on a digital Vickers hardness (XHVT−10Z) indenter at a load of 5 kg for a dwell time of 15 s, and each hardness value shown afterward was the mean value of 5 parallel tests. Tensile tests were performed on a universal testing machine (Zwick/Roell Z100) at a speed of 1 mm/min and mean values of 3 parallel tests were used for analysis. The sketch of the tensile samples is shown in Fig. 1(b).

3 Results

3.1 As-cast microstructure

Figure 2 exhibits the XRD pattern of the as-cast Al−*x*Mg−3Zn−1Cu alloys with the standard diffraction patterns of common phases in Al−Mg−Zn−Cu system. Diffraction peaks of η-$MgZn_2$ phase and *S*-Al_2CuMg phase were distinguished on the XRD pattern of Al−3Mg−3Zn−1Cu alloy, while only the diffraction peaks of *T*-$Mg_{32}(AlZn)_{49}$ phase were identified as Mg content exceeded 4 wt.%. The intensity of the diffraction peaks of *T*-$Mg_{32}(AlZn)_{49}$ phase increased as Mg content increased from 4 to 5 wt.%. The above results indicated that the formation of *T*-$Mg_{32}(AlZn)_{49}$ phase was promoted while the formation of η-$MgZn_2$ phase and *S*-Al_2CuMg phase was inhibited with increasing Mg content. As for the structure of the eutectic phase, the η-$MgZn_2$ phase and *S*-Al_2CuMg phase have been confirmed to be hexagonal [14] and orthorhombic [17], respectively, while the structure of *T*-$Mg_{32}(AlZn)_{49}$ phase is quite divergent [15,16]. It is generally believed that *T*-$Mg_{32}(AlZn)_{49}$ phase has a cubic structure [32] with the lattice parameter a=1.409 nm [15]. However, recent studies also indicated that *T*-$Mg_{32}(AlZn)_{49}$ phase may have an icosahedral quasicrystal structure [15,16,32].

Figure 3 illustrates the STA curves of the as-

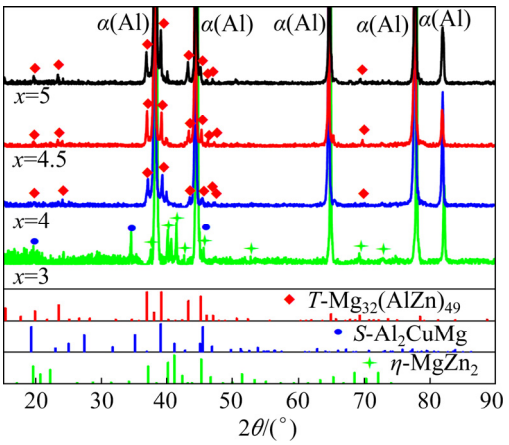

Fig. 2 XRD patterns of as-cast Al−*x*Mg−3Zn−1Cu alloys with standard diffraction patterns of common phases in Al−Mg−Zn−Cu system

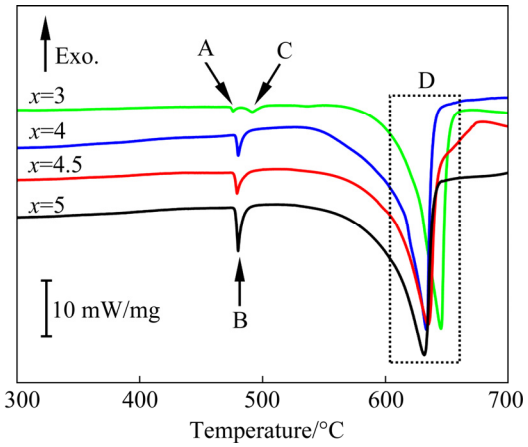

Fig. 3 STA curves of as-cast Al−*x*Mg−3Zn−1Cu alloys

cast Al−*x*Mg−3Zn−1Cu alloys. Four endothermic peaks (severally labeled as A, B, C and D) are distinguished, and the temperature (T_p) and reaction enthalpy (ΔH_R) corresponding to each peak are listed in Table 2. Three endothermic peaks were severally observed at 476 °C (Peak A), 492 °C (Peak C), and 645 °C (Peak D) on the STA curve of Al−3Mg−3Zn−1Cu alloy. As Mg content increased to 4 wt.%, Peaks A and C disappeared, while another endothermic peak near 480 °C (Peak B) emerged. The intensity of Peak B increased as Mg content increased from 4 to 5 wt.%. The temperature corresponding to Peak D decreased from 645 to 632 °C as Mg content increased from 3 to 5 wt.%. Among these peaks, Peaks A, B and C were associated with the melting of eutectic phases while Peak D corresponded to the melting of α(Al). Although the temperature difference between Peaks A and B is very small (less than 4 °C), they may belong to different phases. Extensive studies suggested that the melting temperature of η-$MgZn_2$ phase fluctuates around 475 °C with a small deviation [14,18,19], the melting temperature of T-$Mg_{32}(AlZn)_{49}$ phase is between 480 and 485 °C [12], and the melting temperature of S-Al_2CuMg phase fluctuates around 490 °C [19]. Combined with the XRD results, Peaks A, B, and C correspond to the melting of η-$MgZn_2$ phase, T-$Mg_{32}(AlZn)_{49}$ phase, and S-Al_2CuMg phase, respectively.

Figure 4 shows the microstructure of the as-cast Al−*x*Mg−3Zn−1Cu alloys, and the statistics values of the as-cast alloys are shown in Fig. 5. The as-cast alloys consist of α(Al) equiaxed dendrites and eutectic phase elongating along grain boundaries and inter-dendritic regions (Figs. 4(a−d)). The grain size statistics in Fig. 5(a) suggested that the grains were refined from 135 to 90 μm as Mg content increased from 3 to 5 wt.%. This is consistent with the observations of MONDAL and MUKHOPADHYAY [33]. The distribution of the eutectic phase was transformed from intermittent in Al−3Mg−3Zn−1Cu alloy to continuous when Mg content exceeded 4 wt.%. As Mg content increased from 3 to 5 wt.%, the fraction and size of the eutectic phase increased from 2.2% to 5.8% and from 6.2 to 10.8 μm, respectively (Fig. 5(b)).

The characteristic of the eutectic phase in the as-cast alloys is shown in Fig. 6, and the EDS results of the eutectic phase are given in Table 3. Two categories of eutectic phases are distinguished by morphology distinction in Al−3Mg−3Zn−1Cu alloy (Fig. 6(a)). The vimineous phases are mainly distributed at grain boundaries, while the elliptical phases are mainly interspersed within grains. The difference in eutectic phase distribution was also observed in similar alloys [33,34]. EDS results indicate that eutectic phases are formed by co-segregation of Al, Mg, Zn and Cu elements. The vimineous phases have the composition of 28 at.% Mg, 40.58 at.% Al, 14.55 at.% Zn and 16.87 at.% Cu. Combined with the XRD and STA

Table 2 Temperature (T_p) and reaction enthalpy (ΔH_R) corresponding to endothermic peaks on STA curves of as−cast Al−*x*Mg−3Zn−1Cu alloys

x	Peak A		Peak B		Peak C		Peak D	
	T_p/°C	ΔH_R/(J·g^{-1})	T_p/°C	ΔH_R/(J·g^{-1})	T_p/°C	ΔH_R/(J·g^{-1})	T_p/°C	ΔH_R/(J·g^{-1})
3	476	2.26	–	–	492	5.94	645	879.88
4	–	–	480	12.51	–	–	633	1075.84
4.5	–	–	479	18.24	–	–	634	1006.86
5	–	–	480	29.34	–	–	632	901.63

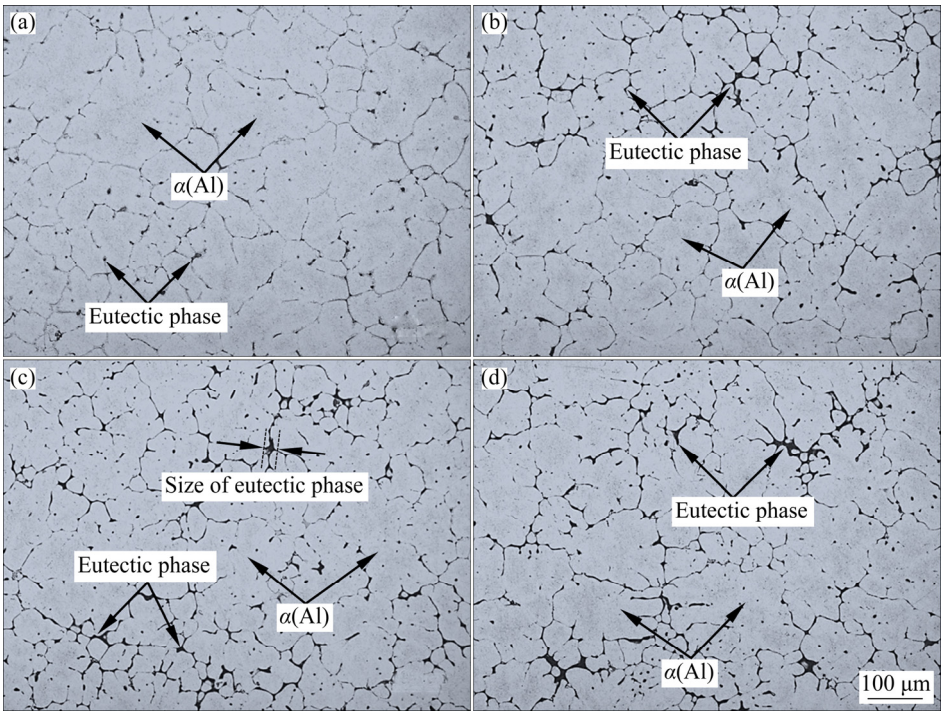

Fig. 4 Microstructures of as-cast Al−*x*Mg−3Zn−1Cu alloys: (a) *x*=3; (b) *x*=4; (c) *x*=4.5; (d) *x*=5

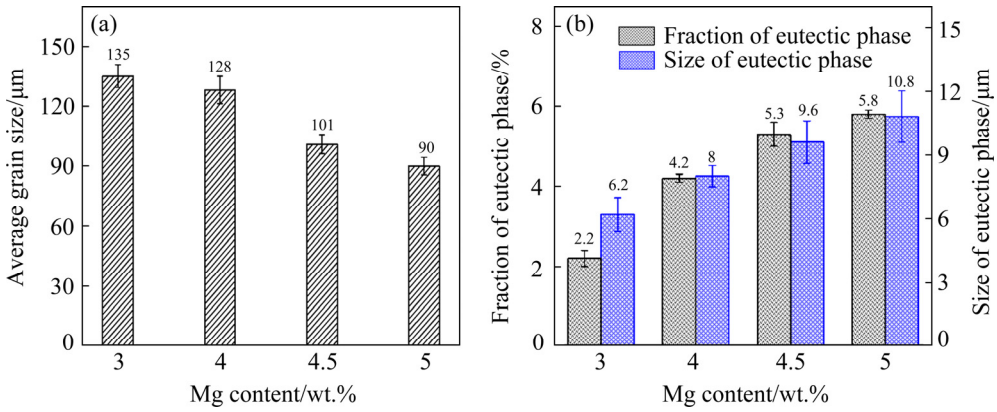

Fig. 5 Statistics of as-cast Al−*x*Mg−3Zn−1Cu alloys: (a) Average grain size; (b) Fraction and size of eutectic phase

results, it is legitimate to designate this phase to η-Mg(AlZnCu)$_2$ phase; namely, parts of Zn atoms in the η-MgZn$_2$ phase are replaced by Al and Cu atoms. The element contents in the elliptical phase are 9.37 at.% Mg, 79.25 at.% Al, 4.95 at.% Zn and 6.43 at.% Cu. This phase has equivalent Mg and Cu contents and is most probably eutectic *S*-Al$_2$CuMg phase according to the XRD and STA results. When Mg content exceeded 4 wt.%, the vimineous η-Mg(AlZnCu)$_2$ phase and elliptical *S*-Al$_2$CuMg phase disappeared, while another eutectic phase with lamellar or curly morphology emerged (Figs. 6(b−d)). The network of this eutectic phase became more and more continuous and concentrated as Mg content increased. This phase has an approximate composition of 33 at.% Mg, 47 at.% Al, 10 at.% Zn and 9.5 at.% Cu, most probably *T*-Mg$_{32}$(AlZnCu)$_{49}$ phase, and namely, the *T*-Mg$_{32}$(AlZn)$_{49}$ phase in which parts of Al and Zn atoms are replaced by Cu atoms. Notably, the composition of the eutectic phases in this study deviated from the standard composition to some degree, which is attributed to the mutual substitution of atoms in these phases [14,21,33].

3.2 Microstructural evolution during solution treatment

Based on the STA results in Fig. 3 and Table 2, it is appropriate to set 470 °C as the solution treatment temperature to prevent from overburning.

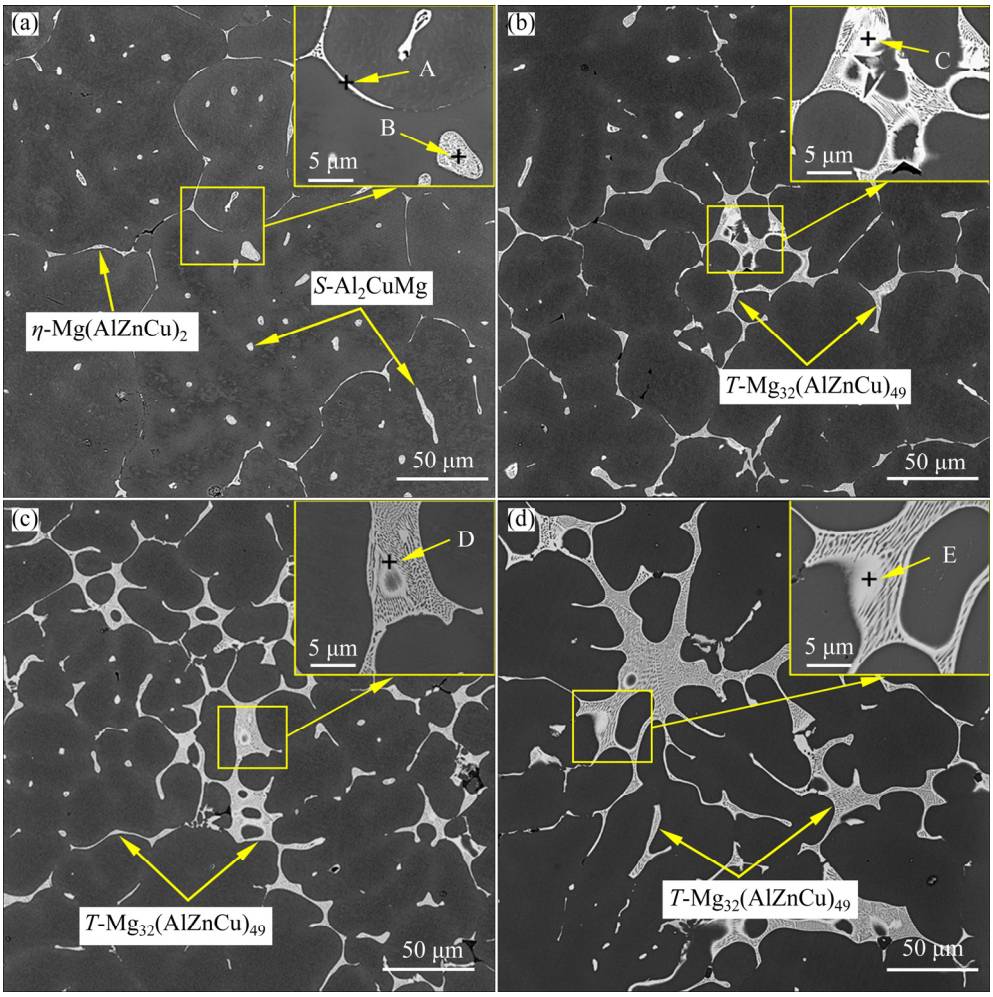

Fig. 6 SEM images of as-cast Al−*x*Mg−3Zn−1Cu alloys: (a) *x*=3; (b) *x*=4; (c) *x*=4.5; (d) *x*=5

Table 3 Chemical compositions at marked positions in Fig. 6

Position	Content/at.%				Phase
	Mg	Al	Zn	Cu	
A	28.00	40.58	14.55	16.87	η-Mg(AlZnCu)$_2$
B	9.37	79.25	4.95	6.43	*S*-Al$_2$CuMg
C	34.95	44.32	10.89	9.85	*T*-Mg$_{32}$(AlZnCu)$_{49}$
D	31.99	49.16	9.66	9.19	*T*-Mg$_{32}$(AlZnCu)$_{49}$
E	33.68	47.08	9.85	9.39	*T*-Mg$_{32}$(AlZnCu)$_{49}$

Figure 7 shows the evolution of the eutectic phase during solution treatment at 470 °C by taking Al−5Mg−3Zn−1Cu alloy as an example, illustrating the fragmentation, disintegration, spheroidization, and dissolution of the eutectic phase [28,35]. After 1 h of solution treatment, the fragmentation of the eutectic framework started. With the solution treatment proceeding (2 h), the small-scaled phases dissolved directly, while the bulky phases disintegrated gradually. After 4 h of solid solution, the large eutectic network was completely replaced by small particles induced by the disintegration. Dissolution tended to be mild subsequently, and these small pieces were gradually spheroidized and dissolved in subsequent process. By 12 h, most of the eutectic phase has dissolved into the matrix. The dissolution of the eutectic phase tended to be complete after 24 h of solution treatment, and the microstructure did not change visibly anymore when the solution was further extended to 36 h.

The evolution of the fraction of eutectic phase during solution treatment is illustrated in Fig. 8. The fraction of eutectic phase reduced drastically in the preliminary stage of solution treatment, and then dissolution slowed down until it gradually reached a relative balance state where the ratio of the residual eutectic phase to the original eutectic phase was lower than 5%, which means that the eutectic phase has dissolved into α(Al) matrix sufficiently. The

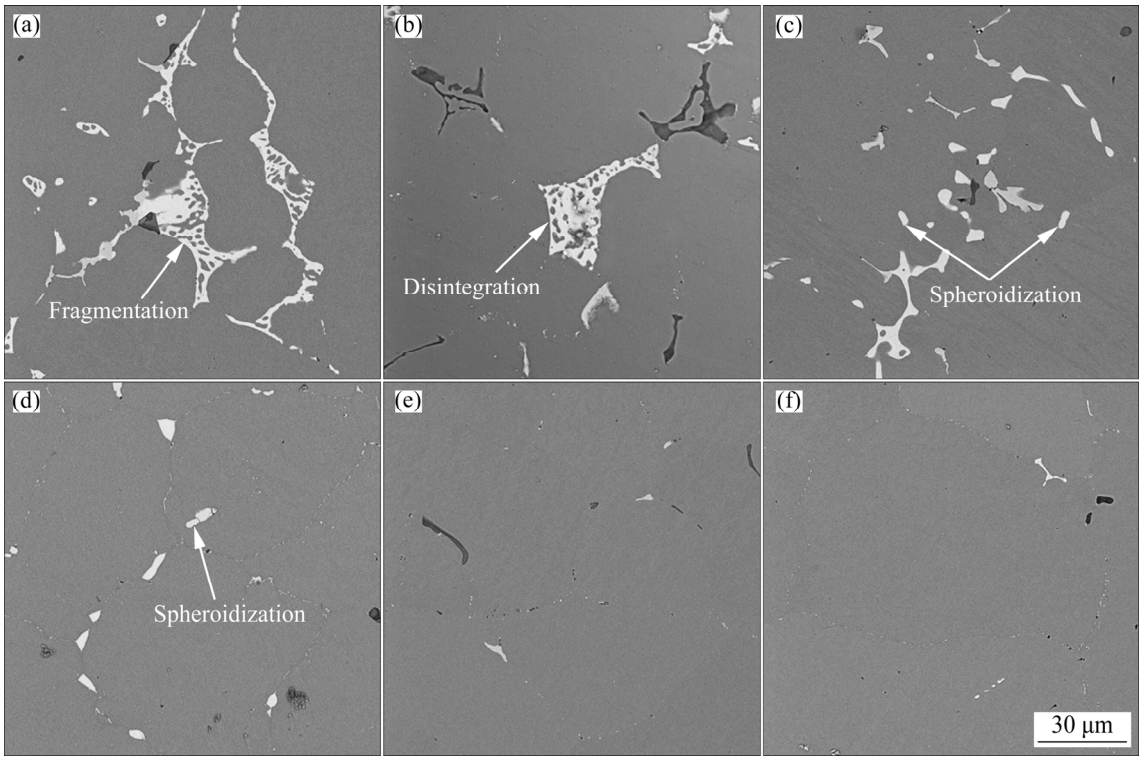

Fig. 7 Microstructural evolution of Al−5Mg−3Zn−1Cu alloys during solution treatment at 470 °C for 1 h (a), 2 h (b), 4 h (c), 12 h (d), 24 h (e) and 36 h (f)

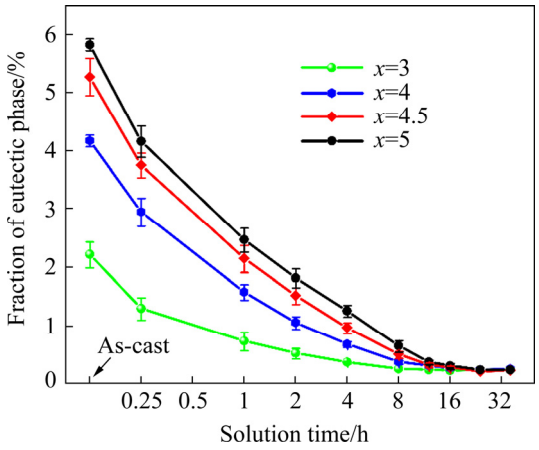

Fig. 8 Fraction of eutectic phase in Al−*x*Mg−3Zn−1Cu alloys during solution treatment at 470 °C

time required for the complete dissolution of the eutectic phase increased from 8 to 24 h as Mg content increased from 3 to 5 wt.%.

Figure 9 shows the microstructure of Al−*x*Mg−3Zn−1Cu alloys after solution treatment at 470 °C for 24 h, and the XRD patterns and statistics of grain size are shown in Fig. 10. The eutectic phase at grain boundaries disappeared, and accordingly, the diffraction peaks corresponding to the eutectic phases on the XRD patterns vanished (Fig. 10(a)), indicating that the eutectic phases have dissolved into matrix adequately. The grain sizes of the alloys after solution treatment are 139, 132, 105, and 93 μm, respectively (Fig. 10(b)), indicating that the solution process did not lead to obvious grain coarsening.

3.3 Age-hardening response

Figures 11(a, c, e) show the age-hardening curves of Al−*x*Mg−3Zn−1Cu alloys aged at 120, 150 and 175 °C, respectively. The corresponding age-hardening rate curves are derivated by differentiating the age-hardening curves and are shown in Figs. 11(b, d, f). When aged at 120 °C (Figs. 11(a, b)), rapid hardening was observed within the first 0.5 h, and the hardening rate reached 7.2, 15.8, 36.8 and 60.6 HV/h for the four alloys in the preliminary stage, respectively. The age-hardening curves entered a transition zone (0.5−10 h) where the hardening rate slackened with the extension of aging time. The hardness rose slowly subsequently to the peak-aged hardness and decreased slightly with the prolongation of aging time. The time required to reach the peak-aged state extended from 64 h for Al−3Mg−3Zn−1Cu alloy

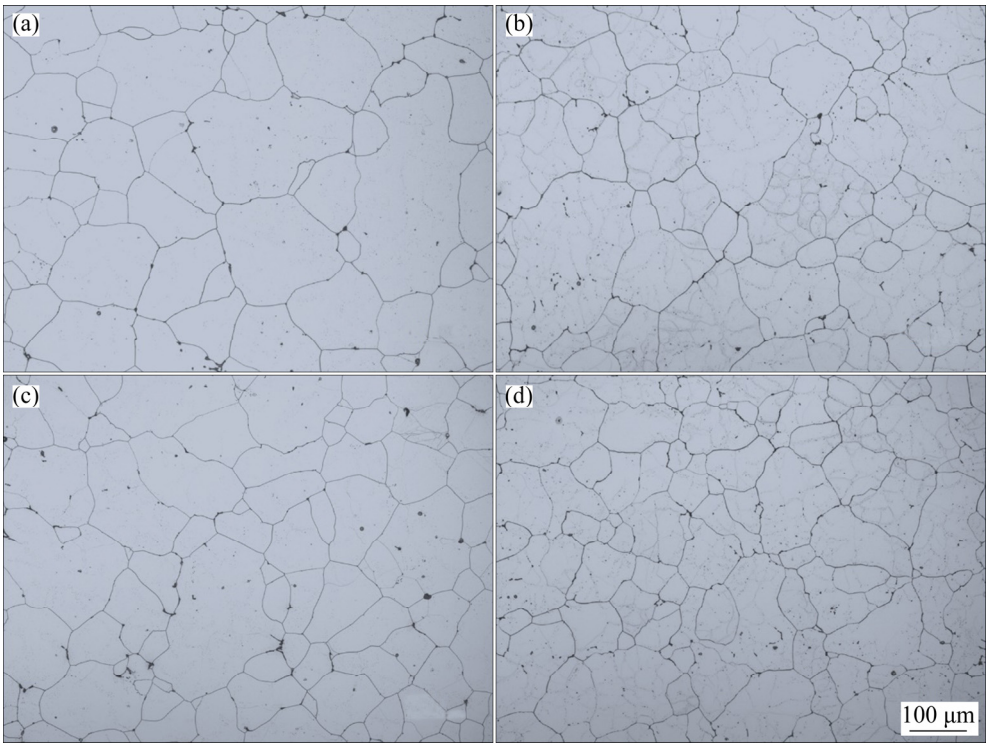

Fig. 9 Microstructures of Al−*x*Mg−3Zn−1Cu alloys after solution treatment at 470 °C for 24 h: (a) *x*=3; (b) *x*=4; (c) *x*=4.5; (d) *x*=5

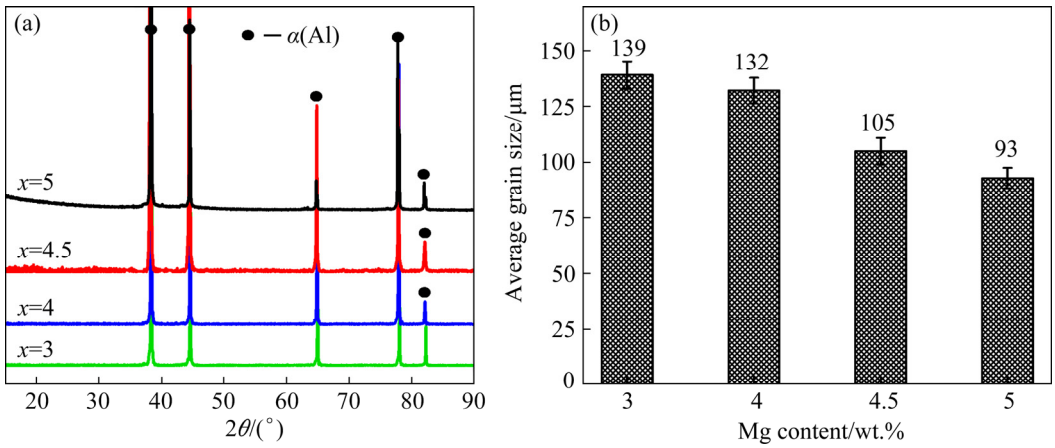

Fig. 10 XRD patterns (a), and grain size statistics (b) of Al−*x*Mg−3Zn−1Cu alloys after solution treatment at 470 °C for 24 h

and Al−4Mg−3Zn−1Cu alloy to 96 h for Al−4.5Mg−3Zn−1Cu alloy and Al−5Mg−3Zn−1Cu alloy. Naturally, alloy with higher Mg content has a higher hardness at any time.

When aged at 150 °C (Figs. 11(c, d)), rapid hardening was still observed in the preliminary stage of aging when Mg content exceeded 4 wt.% (0−0.5 h). The increase of aging temperature resulted in a distinct increase in the hardening rate, and the initial hardening rate increased from 14.4 HV/h for Al−4Mg−3Zn−1Cu alloy to 94.4 HV/h for Al−5Mg−3Zn−1Cu alloy. However, a negative hardening rate of −18.6 HV/h was observed in the initial stage of aging for Al−3Mg−3Zn−1Cu alloy, indicating that the hardness has a downward trend, which is probably attributed to the reversion of natural aging [36]. The subsequent age hardening resembled that at 120 °C, except that the time required for the four alloys to reach the peak-aged state was shortened to 16 h. The age-hardening at 175 °C (Figs. 11(c, f)) is quite similar to that at 150 °C but the peak aging time was further

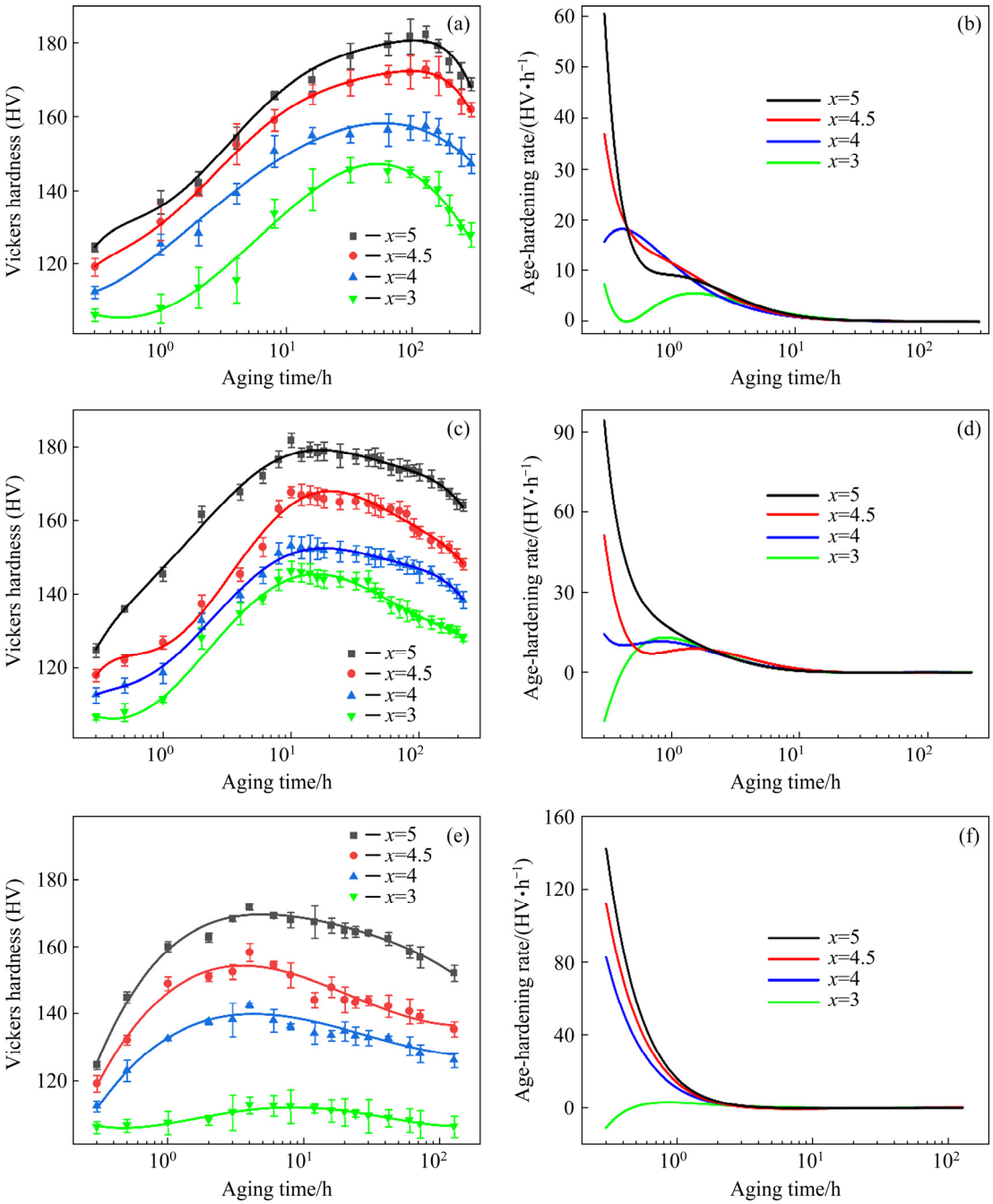

Fig. 11 Aging-hardness curves (a, c, e) and corresponding age-hardening rate curves (b, d, f) of Al−*x*Mg−3Zn−1Cu alloys aged at 120 °C (a, b), 150 °C (c, d) and 175 °C (e, f)

shortened to 4 h. With the increase of aging temperature, the peak hardness of these alloys decreases. Notably, the peak hardness of Al−5Mg−3Zn−1Cu alloy dropped slightly while only weak age-hardening was observed for Al−3Mg−3Zn−1Cu alloy when aged at 175 °C.

3.4 Microstructure of peak-aged alloys

Figure 12 shows the microstructure of the peak-aged Al−*x*Mg−3Zn−1Cu alloys (aged at 150 °C for 16 h). TEM bright-field images in Figs. 12(a−d) indicate that the matrix was occupied by spherical precipitates. The selected area diffraction patterns (SADP) of Al−3Mg−3Zn−1Cu alloys along $[001]_{Al}$ is shown in Fig. 12(e). The diffraction spots at 2/5 and 3/5 $(220)_{Al}$ in the SADP of Al−3Mg−3Zn−1Cu alloy demonstrate that these precipitates are *T′* precipitates [9]. It has also been

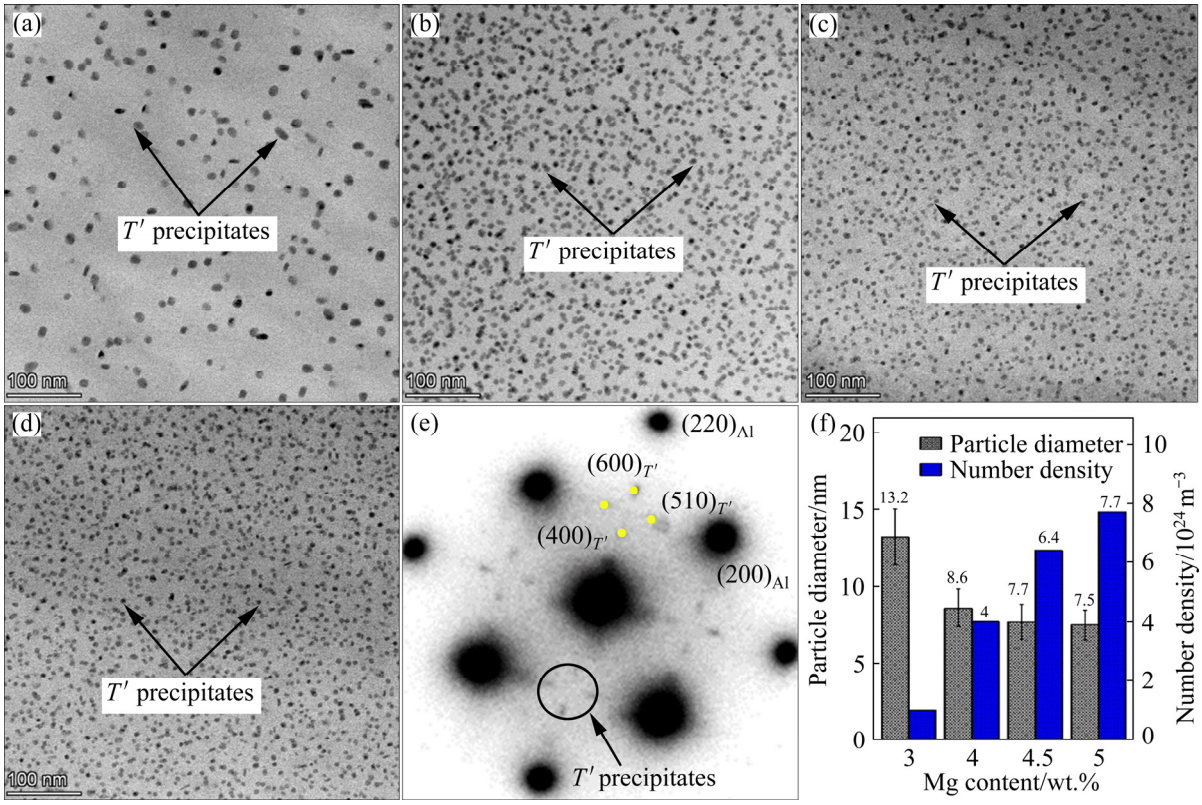

Fig. 12 TEM analysis results of peak-aged Al−*x*Mg−3Zn−1Cu alloys: (a−d) TEM bright-field images; (e) SADP pattern of Al−3Mg−3Zn−1Cu alloy; (f) Size and number density of precipitates

confirmed that the precipitates in Al−5Mg−3Zn−1Cu cast alloy after aging at 150 °C for 16 h are also *T′* precipitates [29]. Therefore, the precipitates in the peak-aged Al−*x*Mg−3Zn−1Cu alloys in this work are metastable *T′* phases and the category of precipitates is not changed with increasing Mg content. Notably, the absence of diffraction spot at 1/3 and 2/3 $(220)_{Al}$ excluded the presence of *η′* precipitates, which are the most common precipitates in peak-aged Al−Mg−Zn−Cu alloys [1,7,8].

The distribution of the precipitates became more and more dispersive and homogeneous with the increment of Mg content (Figs. 12(a−d)). The statistics of the size and number density of the precipitates is presented in Fig. 12(f). The mean diameter of the precipitates decreased rapidly from 13.2 to 8.6 nm as Mg content increased from 3 to 4 wt.%, then decreased gently to 7.7 nm within 0.5 wt.% increment of Mg content, and finally tended to be stable when Mg content exceeded 4.5 wt.%. The number density of the precipitates increased continuously from 1×10^{24} to 7.7×10^{24} m^{-3} as Mg content was elevated from 3 to 5 wt.%.

3.5 Tensile properties

Figure 13 illustrates the tensile properties and representative tensile curves of Al−*x*Mg−3Zn−1Cu alloys under as-cast, solution treated and peak-aged states. As shown in Figs. 13(a, b), the yield strength (YS) and ultimate tensile strength (UTS) of the as-cast alloys increased with increasing Mg content, concretely from 161.1 and 234.5 MPa for Al−3Mg−3Zn−1Cu alloy to 188.3 and 250.8 MPa for Al−5Mg−3Zn−1Cu alloy, respectively. Conversely, the elongation of the as-cast alloys dropped from 3.9% to 2.1% as Mg content increased from 3 to 5 wt.%.

The tensile properties of solution-treated Al−*x*Mg−3Zn−1Cu alloys are shown in Figs. 13(c, d). With the increase of Mg content from 3 to 5 wt.%, the YS and UTS increased significantly, from 105.4 to 198.1 MPa and from 246 to 342.3 MPa, respectively, while the elongation of the alloys decreased from 29.4% to 18.6%.

The tensile properties of the peak-aged Al−*x*Mg−3Zn−1Cu alloys (aged at 150 °C for 16 h) are depicted in Figs. 13(e, f). As Mg content increased from 3 to 5 wt.%, the YS exhibited 57.2%

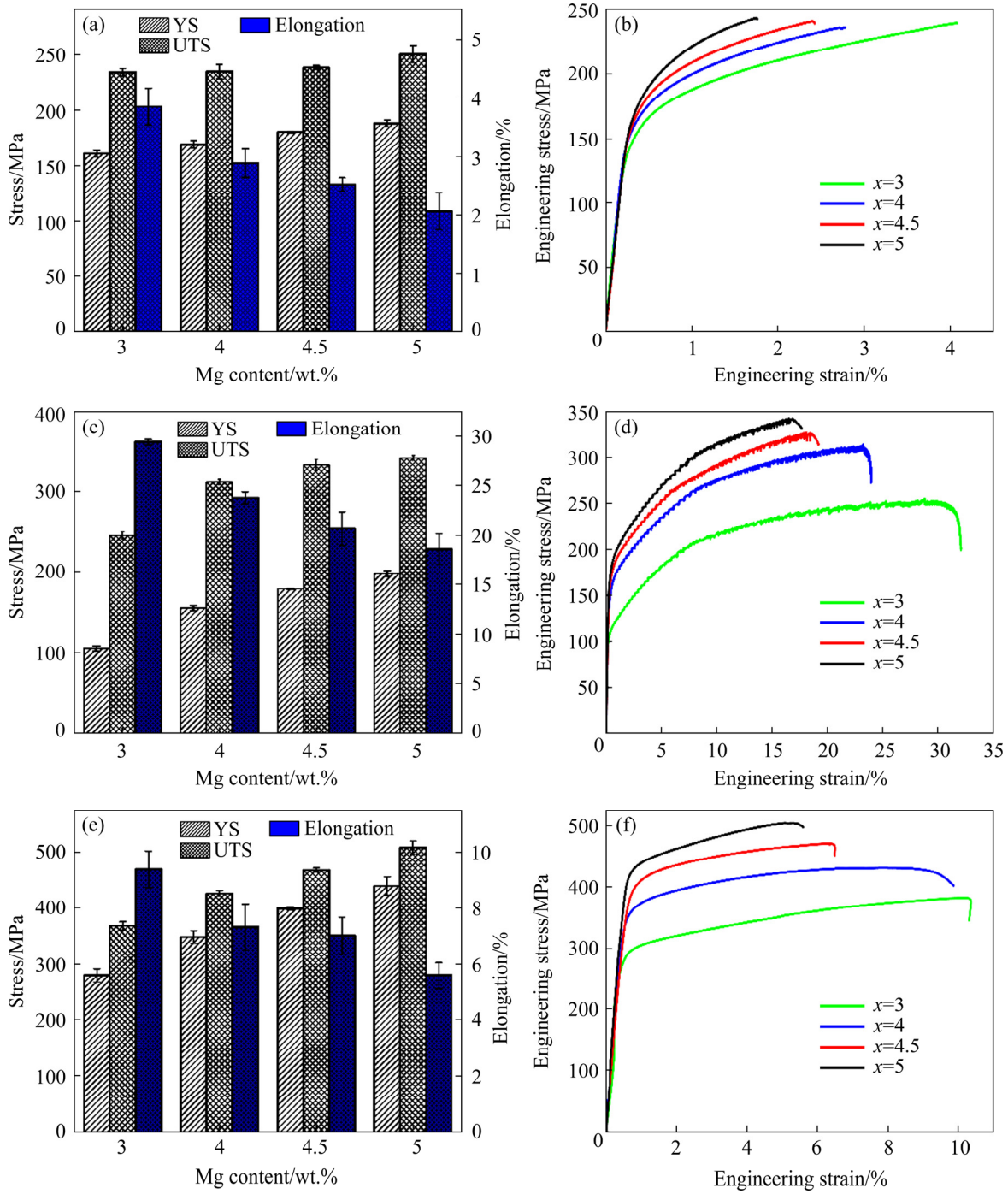

Fig. 13 Tensile properties (a, c, e) and representative tensile curves (b, d, f) of Al−*x*Mg−3Zn−1Cu alloys under different heat treatment state: (a, b) As-cast; (c, d) Solution treated; (e, f) Aged at 150 °C for 16 h

increment, from 279.5 to 439.4 MPa and the UTS exhibited 38.2% increment, from 368 to 508.5 MPa, while the elongation of the alloys dropped from 9.4% to 5.6%. Compared with the corresponding solution-treated alloys, the UTS was increased by 49.6%, 36.6%, 40.36% and 48.6%, respectively, while the elongation dropped dramatically. Compared with the as-cast alloys, the UTS was increased by 56.9%, 81.2%, 96.2% and 102.8%, respectively, indicating that the alloys own extraordinary aging hardening potential.

The strength−elongation collation map of the peak-aged Al−*x*Mg−3Zn−1Cu alloys and several previously reported gravity cast Al−Zn−Mg−Cu alloys is depicted in Fig. 14. Although the strength of Al−*x*Mg−3Zn−1Cu alloys in this work is not

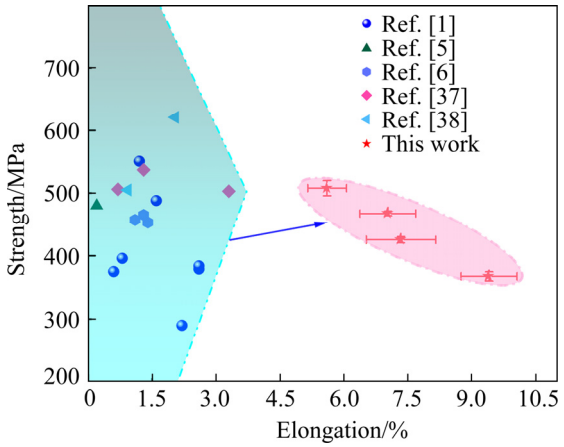

Fig. 14 Strength−elongation collation map of peak-aged Al−*x*Mg−3Zn−1Cu alloys in this work and previously reported gravity cast Al−Zn−Mg−Cu alloys [1,5,6,37,38]

particularly high, these alloys present superior elongation, demonstrating that Al−*x*Mg−3Zn−1Cu cast alloys have a good synergy of strength and ductility, especially Al−4.5Mg−3Zn−1Cu alloy and Al−5Mg−3Zn−1Cu alloys.

3.6 Fractography

Figure 15 depicts the tensile fractography of the peak-aged Al−*x*Mg−3Zn−1Cu alloys. As illustrated in Figs. 15(a−c), dimples and tear ridges are observed synchronously on the fracture surface when Mg content is less than 4.5 wt.%, revealing that mixed fracture is the predominant fracture mechanism [39]. Conversely, typical intergranular fracture morphology is presented on the fracture surface of Al−5Mg−3Zn−1Cu alloy, and secondary cracks are also observed to propagate along grain boundaries (Fig. 15(d)), revealing that intergranular fracture is the dominant mechanism. The above analysis indicates that the fracture mode of peak-aged Al−*x*Mg−3Zn−1Cu alloys is converted from mixed fracture to intergranular fracture as Mg content exceeds 4.5 wt.%.

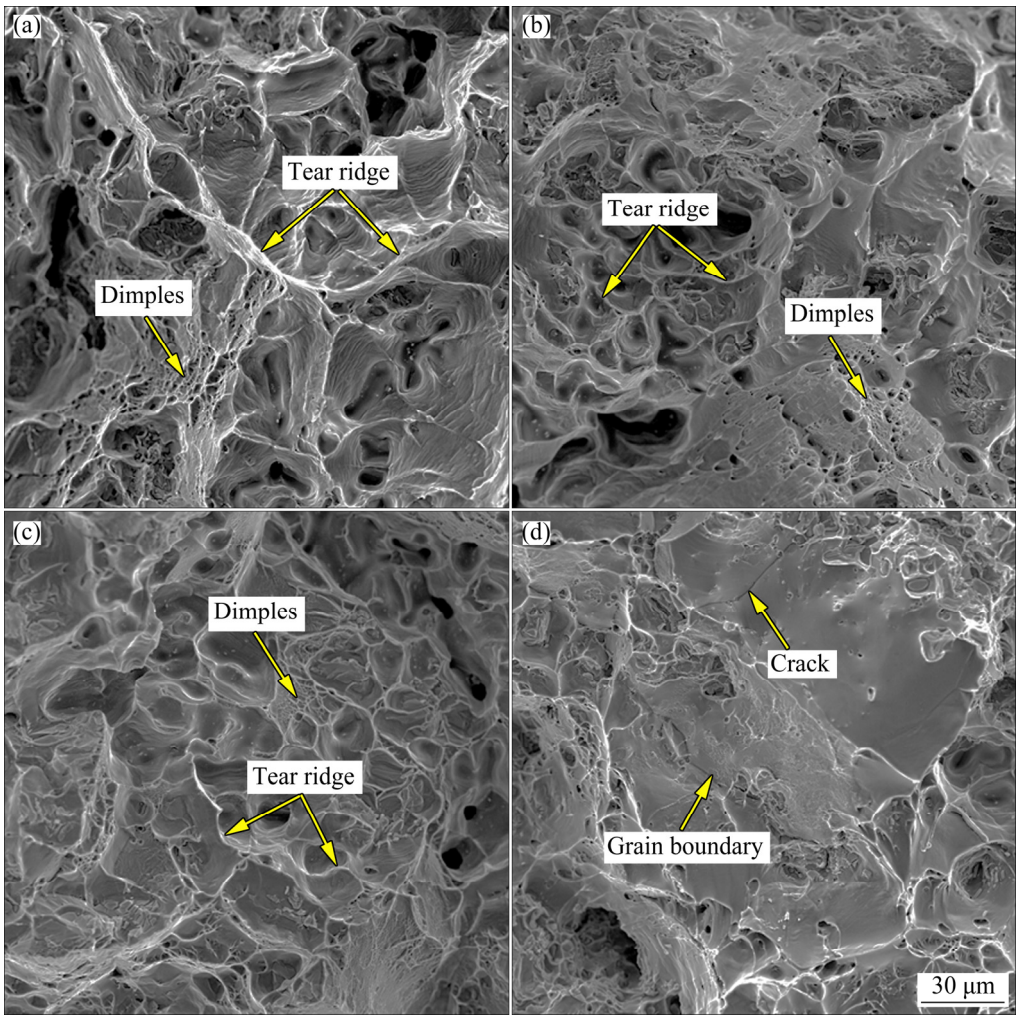

Fig. 15 Tensile fractographs of peak-aged Al−*x*Mg−3Zn−1Cu alloys: (a) *x*=3; (b) *x*=4; (c) *x*=4.5; (d) *x*=5

4 Discussion

4.1 Effects of Mg content on grain refinement

The grain size statistics demonstrated that the grains of the alloys were refined by increasing Mg addition (Fig. 5), which is consistent with the study of as-cast Al−(0.06−32.0)Mg alloys [40] and Al−8.0Zn−(1.8−2.3)Mg−(2.0−2.6)Cu alloys [33]. The mechanism of grain refinement by increasing Mg content is ascribed to the enhanced growth restriction [41] as quantified in Eq. (1):

$$Q=\left[\frac{\partial(\Delta T_{\mathrm{CS}})}{\Delta f_{\mathrm{s}}}\right]_{f_{\mathrm{s}}\to 0}\approx\sum m_i c_{0,i}(k_i-1) \tag{1}$$

where Q is the growth restriction factor, ΔT_{CS} is constitutional supercooling, f_{s} is solid fraction, m_i, $c_{0,i,}$ and k_i are severally liquidus slope, concentration and equilibrium partition coefficient of solute i. ΔT_{CS} and Q for Al−xMg−3Zn−1Cu alloys are calculated by Pandat package based on Scheil model and the results are shown in Fig. 16. As Mg content was increased from 3 to 5 wt.%, Q induced by constitutional supercooling increased monotonously from 16.27 to 24.73 K, thereby resulting in grain refinement [42]. This mechanism is supported by the microstructure observation that the solute-rich eutectic phase at grain boundaries is gradually enriched with the increment of Mg content (Figs. 4(a−d)).

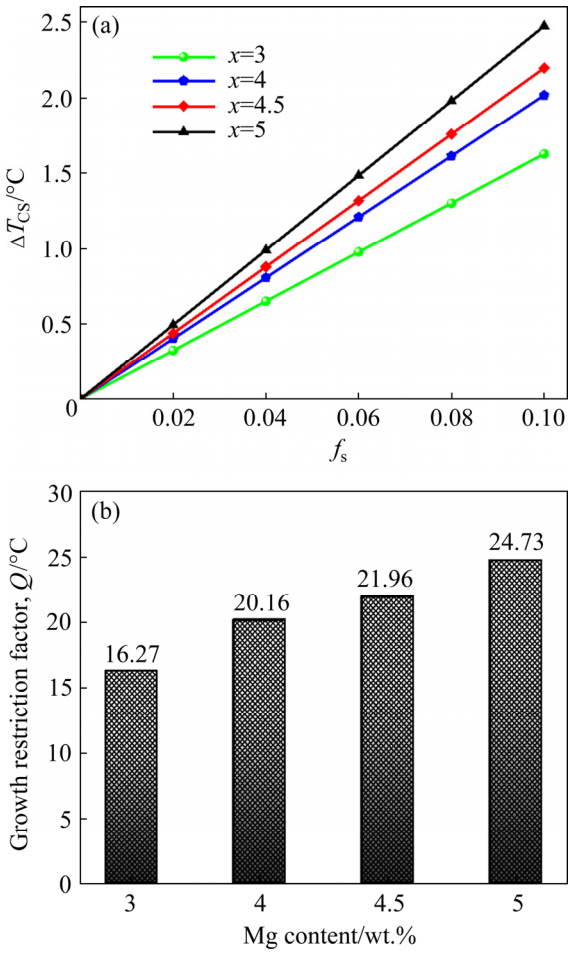

Fig. 16 Constitutional supercooling ΔT_{CS} (a) and growth restriction factors Q (b) in preliminary stage of solidification of Al−xMg−3Zn−1Cu alloys

4.2 Effects of Mg content on solution kinetics

The microstructural evolution and statistics indicated that the solution kinetics of Al−xMg−3Zn−1Cu alloys was evidentially affected by Mg content. Researches suggested that secondary dendrite arm spacing and size of eutectic phase are two critical factors affecting the solution process [14,43]. In this study, the size of eutectic phase seems to be the crucial one because secondary dendrites were not well developed in the alloys. In the initial stage of solid solution, the eutectic phase dissolves to the adjacent matrix quickly, and then the dissolution slows down due to the increase of supersaturation in the matrix. The higher the Mg content is, the coarser the eutectic phase is, and in turn the more serious the blockage of the solute in the adjacent matrix is and the slower the dissolution of the eutectic phase is. ZOLOTOREVSKII and TELESHOV [44] gave an expression of the time required for complete dissolution of the eutectic phase (τ) as a function of the size of the eutectic phase (m):

$$\tau=am^n \tag{2}$$

where a and n are parameters varying with the categories of alloys, and n is between 1.5 and 2.5 for Al alloys [14]. The function between the time required for complete dissolution of the eutectic phase and the size of the eutectic phase is established by fitting the experimental data in Fig. 17:

$$\tau=0.2m^{2.06} \tag{3}$$

The average size of eutectic phase increased by 74% as Mg content increased from 3 to 5 wt.% (Fig. 3). Thus, the time required for the eutectic phase to completely dissolve into the α(Al) matrix was tripled, as inferred from Eq. (3), and this echoes the results in Fig. 7.

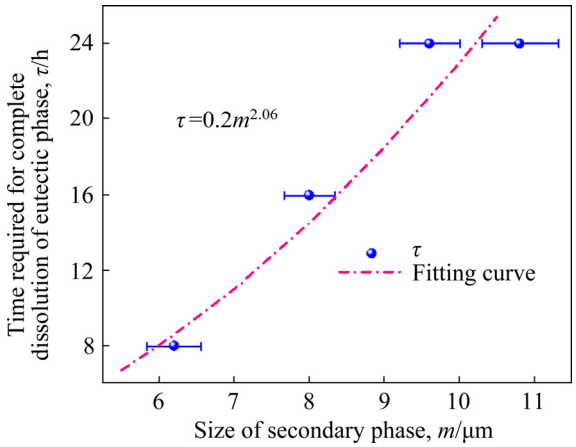

Fig. 17 Relationship between time required for complete dissolution of eutectic phase and size of eutectic phase

4.3 Effects of Mg content on age-hardening and precipitation behavior

As illustrated in Fig. 11, the hardness elevation of Al–*x*Mg–3Zn–1Cu alloys is mainly reflected in the early stage of aging, which is consistent with age-hardening of Al–6.3Zn–3Mg–1.8Cu–(Sc,Zr) alloys [16]. Hardening in the early stage of aging is undoubtedly closely related to the inchoate precipitation behavior, which is accelerated with the increment of Mg content (Fig. 11) [24]. It is well known that precipitation during aging is a vacancy-mediated solute diffusion process [45]. In the early stage of aging, a large number of solute clusters are formed and act as precursors of GP zones and T' precipitates [31,46]. The number of precursors in the alloy increases with the increase of Mg content [7], thereby accelerating and promoting the subsequent age-hardening. Solute clusters can act as prisons to confine the quenching vacancies [47]. However, the quenching vacancies annihilate in the first few seconds when aged at high temperatures [45]. Alloys with a lower Mg content cannot imprison enough vacancies in the early stage of aging at high temperature, and therefore exhibit an infirm aging hardening response. The age-hardening curve of Al–3Mg–3Zn–1Cu alloy at 175 °C is a typical example (Fig. 11(e)). Similar phenomena have also been observed in Al–6.5Zn–2.3Mg–2.1Cu alloy [48].

Different from the conventional low Mg-containing Al–Mg–Zn–Cu alloys with high Zn content, the precipitates in the peak-aged Al–*x*Mg–3Zn–1Cu alloys in this work are T' precipitates rather than η' precipitates. Analogous results have been found in similar alloys [10,49]. The category of precipitates in peak-aged Al–Mg–Zn–Cu alloys is highly dependent on the Zn/Mg ratio. The study by ZOU et al [9] showed that η' precipitates exist in the peak-aged Al–Mg–Zn–Cu alloys when the Zn/Mg ratio is not less than 2.24. However, the maximum Zn/Mg ratio of the alloys involved in this study is 1, which is much smaller than the above-mentioned threshold. Therefore, the T' precipitates are the exclusive precipitates in the peak-aged Al–*x*Mg–3Zn–1Cu cast alloys involved in this work and similar alloys [49].

4.4 Analysis of strengthening mechanisms

For the peak-aged Al–*x*Mg–3Zn–1Cu cast alloys, the increment in yield strength (σ_y) comes from grain boundary strengthening, solid solution strengthening, and precipitation strengthening.

The grain boundary strengthening is calculated by the Hall–Petch relationship [50]:

$$\sigma_{gb} = \sigma_\alpha + k \cdot d_{gs}^{-1/2} \tag{4}$$

where σ_{gb} is the value of grain boundary strengthening, σ_α (=10 MPa) is the intrinsic strength of pure aluminum, k (=0.065 MPa·m$^{-1/2}$) is the Hall–Petch coefficient and d_{gs} represents grain size [9]. Assuming that artificial aging does not cause grain growth, based on the grain size statistics (Fig. 10), values of grain boundary strengthening are 15.5, 15.7, 16.4 and 16.8 MPa, respectively.

According to studies of LABUSCH [51] and SHERCLIFF and ASHBY [52], solution strengthening can be quantified by

$$\sigma_{ss} = \sum A_i \cdot c_i^{2/3} \tag{5}$$

where A_i is the solution strengthening coefficient and the values of A_i for Mg, Zn and Cu are 20.481, 3.085, and 12.431, respectively [53]. c_i is the solute concentration in the matrix for element i, which can be derived from mass conservation [2]:

$$c_i^{alloy} = f_v c_i^{precipitate} + (1 - f_v) c_i \tag{6}$$

where c_i^{alloy} and $c_i^{precipitate}$ are the concentrations of solute i in alloy and precipitates, respectively, and f_v is the volume fraction of precipitates, which is calculated by Eq. (7):

$$f_v = \frac{V_{precipitate}}{V_{total}} \approx \frac{4\pi N r^3}{3At} \tag{7}$$

For the analyzed regions, V_{total} and $V_{precipitate}$ are the volumes of the regions and the volume occupied by precipitates, N is the number of precipitates, and r is the average radius of the precipitates, and A and t represent the projection area and thickness of the region, respectively. Assuming that t=80 nm, then f_v is calculated based on the statistics of the precipitates. Based on previous studies [13], the composition of T' precipitates is 31.36 at.% Mg, 14.42 at.% Zn, 1.65 at.% Cu and 43.94 at.% Al. For convenience, the composition of the precipitates is assumed to be independent of Mg content in the alloy. Based on the above analysis, the concentration of each solute in the matrix is derived, and the solid solution strengthening of the four alloys is quantified to be 58.7, 66.7, 70.4 and 76.4 MPa, respectively.

It is widely accepted that precipitation strengthening in peak-aged Al−Mg−Zn−Cu alloys originates from the Orowan dislocation bypass mechanism [9], and the corresponding increment to yield strength is

$$\sigma_{ppt} = M\frac{0.4Gb}{\pi\lambda_p}\frac{\ln(2\bar{r}/b)}{\sqrt{1-\nu}} \tag{8}$$

where M (=3.06) and G (=26.9 GPa) are the mean orientation factor and shear modulus for FCC polycrystalline matrix, ν (=0.33) is the Poisson ratio, b (=0.286 nm) is the magnitude of Berger's vector, $\bar{r}$ is the mean radius of a circular cross-section in a random plane for spherical precipitates, and λ_p is the edge-to-edge inter-precipitate spacing. The calculated values of the precipitation strengthening of the four alloys are 177.4, 250.1, 291.1 and 315.5 MPa, respectively.

Eventually, the calculated yield strengths of the peak-aged Al−xMg−3Zn−1Cu alloys are 251.6, 332.5, 377.9 and 408.7 MPa, respectively. There is a certain deviation between the calculated and experimental values. The deviation may stem from the lack of precise quantification of precipitates, thereby leading to the misestimation of the solution strength and precipitation strength, but this deviation does not affect the analysis of the strengthening mechanisms. Figure 18 compares the contributions of various strengthening mechanisms at different Mg levels. As presented in Fig. 18(a), the values of grain boundary strengthening and solid solution strengthening increase slightly with the increment of Mg content. Inconsistent with the results of DING et al [49], the precipitation strengthening increased significantly with the elevation of Mg content. As shown in Fig. 18(b), the grain boundary strengthening is limited (less than 7%) and the proportion of solid solution strengthening is between 18.6% and 23.3%, while the contribution of precipitation strengthening is greater than 70%, indicating that the Al−xMg−3Zn−1Cu alloys own excellent age-hardening effect. As Mg content increases, the ratio of grain boundary strengthening and solid solution strengthening drops while the proportion of precipitation strengthening increases, testifying that Mg enhances the precipitation strengthening.

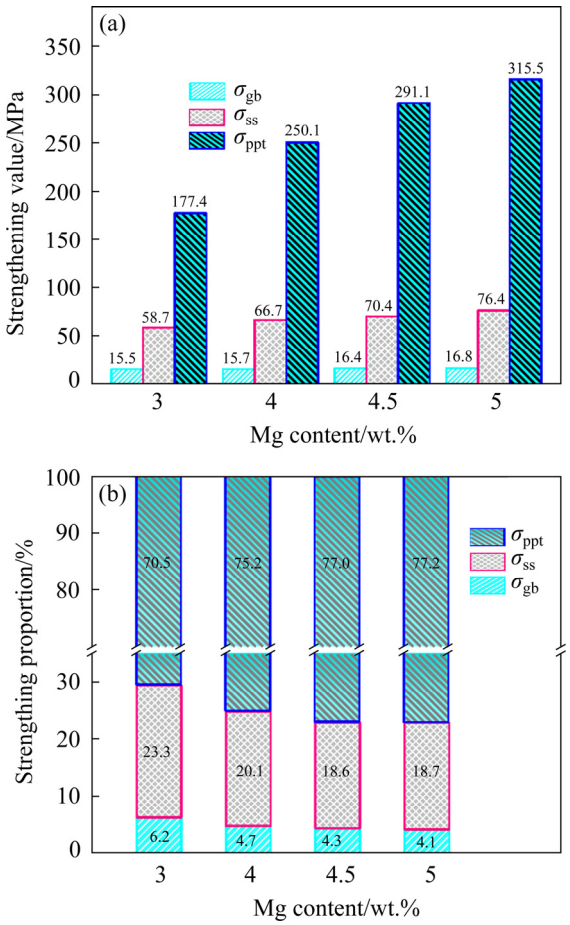

Fig. 18 Values (a) and proportion (b) of different strengthening mechanisms contributing to yield strength of peak-aged Al−xMg−3Zn−1Cu alloys

5 Conclusions

(1) For the as-cast alloys, as Mg content increased from 3 to 5 wt.%, the grains were refined from 135 to 90 μm due to enhanced growth restriction, and the formation of η-Mg(AlZnCu)$_2$

and *S*-Al_2CuMg phases was inhibited while the formation of *T*-$Mg_{32}(AlZnCu)_{49}$ phase was promoted when Mg content exceeded 4 wt.%.

(2) The fraction and size of eutectic phase increased from 2.2% and 6.8 μm to 5.8% and 10.8 μm as Mg content increased from 3 to 5 wt.%, respectively, thereby encumbering the solution kinetics.

(3) Increasing Mg content from 3 to 5 wt.% accelerated and enhanced the age-hardening of the alloys through expediting precipitation rate and elevating the number density of the precipitates. Alloy with a reduced Mg content is more sensitive to aging temperature.

(4) As Mg content increased from 3 to 5 wt.%, the YS and UTS of the as-cast, solution-treated and peak aged alloys were improved, respectively, while the elongation of the alloys decreased. The UTS and elongation of peak-aged Al−5Mg−3Zn−1Cu alloy exceed 500 MPa and 5%, respectively.

(5) Precipitation strengthening implemented by *T′* precipitates is the predominant strengthening mechanism in peak-aged alloys and is enhanced by increasing Mg content.

Acknowledgments

The study is supported by the National Natural Science Foundation of China (Nos. 51674166, U1902220), and the National Key R&D Program of China (No. 2021YFB3701303).

References

[1] GHIAASIAAN R, SHANKAR S. Effect of alloy composition on microstructure and tensile properties of net-shaped castings of Al−Zn−Mg−Cu alloys [J]. International Journal of Metal Casting, 2019, 13: 300−310.

[2] GHIAASIAAN R, SHANKAR S. Structure−property models in Al−Zn−Mg−Cu alloys: A critical experimental assessment of shape castings [J]. Materials Science and Engineering A, 2018, 733: 235−245.

[3] AMIRI M M, FERESHTEH-SANIEE F. Influence of roll speed difference on microstructure, texture and mechanical properties of 7075 aluminum plates produced via combined continuous casting and rolling process [J]. Transactions of Nonferrous Metals Society of China, 2021, 31: 901−912.

[4] XIAO Quan-feng, HUANG Ji-wu, JIANG Ying-ge, JIANG Fu-qin, WU Yun-feng, XU Guo-fu. Effects of minor Sc and Zr additions on mechanical properties and microstructure evolution of Al−Zn−Mg−Cu alloys [J]. Transactions of Nonferrous Metals Society of China, 2020, 30: 1429−1438.

[5] SAIKAWA S, AOSHIMA G, IKENO S, MORITA K, SUNAYAMA N, KOMAI K. Microstructure and mechanical properties of an Al−Zn−Mg−Cu alloy produced by gravity casting process [J]. Archives of Metallurgy and Materials, 2015, 60: 871−874.

[6] SEYED EBRAHIMI S H, AGHAZADEH J, DEHGHANI K, EMAMY M, ZANGENEH S H. The effect of Al−5Ti−1B on the microstructure, hardness and tensile properties of a new Zn rich aluminium alloy [J]. Materials Science and Engineering A, 2015, 636: 421−429.

[7] SHU W X, HOU L G, ZHANG C, ZHANG F, LIU J C, LIU J T, ZHANG L Z, ZHANG J S. Tailored Mg and Cu contents affecting the microstructures and mechanical properties of high-strength Al−Zn−Mg−Cu alloys [J]. Materials Science and Engineering A, 2016, 657: 269−283.

[8] LI Hai-chao, CAO Fu-yang, GUO Shu, JIA Yan-dong, ZHANG Da-yue, LIU Zu-yan, WANG Pei, SERGIO S, SUN Jian-fei. Effects of Mg and Cu on microstructures and properties of spray-deposited Al−Zn−Mg−Cu alloys [J]. Journal of Alloys and Compounds, 2017, 719: 89−96.

[9] ZOU Yan, WU Xiao-dong, TANG Song-bai, ZHU Qian-qian, SONG Hui, GUO Ming-xing, CAO Ling-fei. Investigation on microstructure and mechanical properties of Al−Zn−Mg−Cu alloys with various Zn/Mg ratios [J]. Journal of Materials Science & Technology, 2021, 85: 106−117.

[10] STEMPER L, MITAS B, KREMMER T, OTTERBACH S, UGGOWITZER P J, POGATSCHER S. Age-hardening of high pressure die casting AlMg alloys with Zn and combined Zn and Cu additions [J]. Materials & Design, 2019, 181: 1−11.

[11] LIU Tian-wen, WANG Qu-dong, TANG Hua-ping, LI Zhong-yang, LEI Chuan, MAHMOUD E, JIANG Hai-yan, DING Wen-jiang. Microstructure and mechanical properties of squeeze-cast Al−5.0Mg−3.0Zn−1.0Cu alloys in solution-treated and aged conditions [J]. Transactions of Nonferrous Metals Society of China, 2020, 30: 2326−2338.

[12] TANG Hua-ping, WANG Qu-dong, LUO Colin, LEI Chuan, LIU Tian-wen, LI Zhong-yang, WANG Kui, JIANG Hai-yan, DING Wen-jiang. Effects of solution treatment on the microstructure, tensile properties, and impact toughness of an Al−5.0Mg−3.0Zn−1.0Cu cast alloy [J]. Acta Metallurgica Sinica (English Letters), 2021, 34: 98−110.

[13] TANG Hua-ping, WANG Qu-dong, LEI Chuan, YE Bing, WANG Kui, JIANG Hai-yan, DING Wen-jiang, ZHANG Xiang-feng, LIN Zhen, ZHANG Ji-bin. Effect of cooling rate on microstructure and mechanical properties of an Al−5.0Mg−3.0Zn−1.0Cu cast alloy [J]. Journal of Alloys and Compounds, 2019, 801: 596−608.

[14] LIU Yan, JIANG Da-ming, XIE Wen-long, HU Jie, MA Bo-ran. Solidification phases and their evolution during homogenization of a DC cast Al−8.35Zn−2.5Mg−2.25Cu alloy [J]. Materials Characterization, 2014, 93: 173−183.

[15] VLACH M, ČÍŽEK J, KODETOVÁ V, KEKULE T, LUKÁČ F, CIESLAR M, KUDRNOVÁ J, BAJTOŠOVÁ L, LEIBNER M, HARCUBA P, MÁLEK J, NEUBERT V. Annealing effects in cast commercial Al−Mg−Zn−Cu(−Sc−Zr) alloys [J]. Metals and Materials International, 2021, 27: 995−1004.

[16] VLACH M, KODETOVA V, CIZEK J, LEIBNER M, KEKULE T, LUKÁČ F, CIESLAR M, BAJTOŠOVÁ L, KUDRNOVÁ H, SIMA V, ZIKMUND S, CERNOSKOVA E,

KUTALEK P, NEUBERT V D, NEUBERT V. Role of small addition of Sc and Zr in clustering and precipitation phenomena induced in AA7075 [J]. Metals, 2021, 11: 1−21.

[17] ZHANG J, HUANG Y N, MAO C, PENG P. Structural, elastic and electronic properties of $\theta(Al_2Cu)$ and $S(Al_2CuMg)$ strengthening precipitates in Al−Cu−Mg series alloys: First-principles calculations [J]. Solid State Communications, 2012, 152: 2100−2104.

[18] WANG Shao-hua, MENG Ling-gang, YANG Shou-jie, FANG Can-feng, HAO Hai, DAI Sheng-long, ZHANG Xing-guo. Microstructure of Al−Zn−Mg−Cu−Zr−0.5Er alloy under as-cast and homogenization conditions [J]. Transactions of Nonferrous Metals Society of China, 2011, 21: 1449−1454.

[19] PRIYA P, JOHNSON D R, KRANE M J M. Precipitation during cooling of 7xxx aluminum alloys [J]. Computational Materials Science, 2017, 139: 273−284.

[20] LIU Jun-tao, ZHANG Yong-an, LI Xi-wu, LI Zhi-hui, XIONG Bai-qing, ZHANG Ji-shan. Thermodynamic calculation of high zinc-containing Al−Zn−Mg−Cu alloy [J]. Transactions of Nonferrous Metals Society of China, 2014, 24: 1481−1487.

[21] SHU W X, HOU L G, LIU J C, ZHANG C, ZHANG F, LIU J T, ZHUANG L Z, ZHANG J S. Solidification paths and phase components at high temperatures of high-Zn Al−Zn−Mg−Cu alloys with different Mg and Cu contents [J]. Metallurgical and Materials Transactions A, 2015, 46: 5375−5392.

[22] SHIN J, KIM T, KIM D, KIM D, KIM K. Castability and mechanical properties of new 7XXX aluminum alloys for automotive chassis/body applications [J]. Journal of Alloys and Compounds, 2017, 698: 577−590.

[23] AZARNIYA A, TAHERI A K, TAHERI K K. Recent advances in ageing of 7xxx series aluminum alloys: A physical metallurgy perspective [J]. Journal of Alloys and Compounds, 2019, 781: 945−983.

[24] SHA G, CEREZO A. Early-stage precipitation in Al−Zn−Mg−Cu alloy (7050) [J]. Acta Materialia, 2004, 52: 4503−4516.

[25] HOU Sheng-li, LIU Ping-ping, ZHANG Di, ZHANG Ji-shan, ZHUANG Lin-zhong. Precipitation hardening behavior and microstructure evolution of Al−5.1Mg−0.15Cu alloy with 3.0Zn (wt.%) addition [J]. Journal of Materials Science, 2018, 53: 3846−3861.

[26] KHALFALLAH A, RAHO A A, AMZERT S, DJEMLI A. Precipitation kinetics of GP zones, metastable η' phase and equilibrium η phase in Al−5.46wt.%Zn−1.67wt.%Mg alloy [J]. Transactions of Nonferrous Metals Society of China, 2019, 29: 233−241.

[27] BERG L K, GJØNNES J, HANSEN V, LI X Z, KNUTSON-WEDEL M, WATERLOO G, SCHRYVERS D, WALLENBERG L R. GP-zones in Al−Zn−Mg alloys and their role in artificial aging [J]. Acta Materialia, 2001, 49: 3443−3451.

[28] DENG Yun-lai, WAN Li, ZHANG Yun-ya, ZHANG Xin-ming. Influence of Mg content on quench sensitivity of Al−Zn−Mg−Cu aluminum alloys [J]. Journal of Alloys and Compounds, 2011, 509: 4636−4642.

[29] TANG Hua-ping, WANG Qu-dong, LUO Colin, LEI Chuan, LIU Tian-wen, LI Zhong-yang, JIANG Hai-yan, DING Wen-jiang, FANG Jian, ZHANG Jian-wei. Effects of aging treatment on the precipitation behaviors and mechanical properties of Al−5.0Mg−3.0Zn−1.0Cu cast alloys [J]. Journal of Alloys and Compounds, 2020, 842: 1−12.

[30] BIGOT A, AUGER P, CHAMBRELAND S, BLAVETTE D, REEVES A. Atomic scale imaging and analysis of T' precipitates in Al−Mg−Zn alloys [J]. Microscopy Microanalysis Microstructures, 1997, 8: 103−113.

[31] HOU Sheng-li, ZHANG Di, DING Qing-wei, ZHANG Ji-shan, ZHUANG Lin-zhong. Solute clustering and precipitation of Al−5.1Mg−0.15Cu−xZn alloy [J]. Materials Science and Engineering A, 2019, 759: 465−478.

[32] VLACH M, CIZEK J, KODETOVA V, LEIBNER M, CIESLAR M, HARCUBA P, BAJTOSOVA L, KUDRNOVA H, VLASAK T, NEUBERT V, CERNOSKOVA E, KUTALEK P. Phase transformations in novel hot-deformed Al−Zn−Mg−Cu−Si−Mn−Fe(−Sc−Zr) alloys [J]. Materials & Design, 2020, 193: 1−11.

[33] MONDAL C, MUKHOPADHYAY A K. On the nature of $T(Al_2Mg_3Zn_3)$ and $S(Al_2CuMg)$ phases present in as-cast and annealed 7055 aluminum alloy [J]. Materials Science and Engineering A, 2005, 391: 367−376.

[34] LIU Fu-chu, ZHU Xiang-zhen, JI Shou-xun. Effects of Ni on the microstructure, hot tear and mechanical properties of Al−Zn−Mg−Cu alloys under as-cast condition [J]. Journal of Alloys and Compounds, 2020, 821: 1−11.

[35] EIVANI A R, AHMED H, ZHOU J, DUSZCZYK J. Modeling the TDFD dissolution of Al−Fe−Mn−Si particles in an Al−4.5Zn−1Mg alloy [J]. Philosophical Magazine, 2010, 90: 2865−2897.

[36] LIU Chun-hui, FENG Zhuang-zhuang, MA Pei-pei, ZHOU Yi-hui, LI Guo-hui, ZHAN Li-hua. Reversion of natural ageing and restoration of quick bake-hardening response in Al−Zn−Mg−Cu alloy [J]. Journal of Materials Science & Technology, 2021, 95: 88−94.

[37] YANG Guang-yu, LIU Shao-jun, JIE Wan-qi. Effects of minor Sc addition on the microstructures and mechanical properties of Al−Zn−Mg−Cu casting aluminum alloy [J]. Light Metals, 2016: 463−467.

[38] UTAMI N P E, CHANDRA H. Mechanical properties analysis of Al−9Zn−5Cu−4Mg cast alloy by T5 heat treatment [J]. MATEC Web of Conferences, 2017, 101: 1−6.

[39] LIU Yan, JIANG Da-ming, LI Bing- qing, YANG Wen-shu, HU Jie. Effect of cooling aging on microstructure and mechanical properties of an Al−Zn−Mg−Cu alloy [J]. Materials & Design, 2014, 57: 79−86.

[40] BIROL Y. Effect of solute Mg on grain size of aluminium alloys [J]. Materials Science and Technology, 2012, 28: 924−927.

[41] QUESTED T E, DINSDALE A T, GREER A L. Thermodynamic modelling of growth-restriction effects in aluminium alloys [J]. Acta Materialia, 2005, 53: 1323−1334.

[42] SCHMID-FETZER R, KOZLOV A. Thermodynamic aspects of grain growth restriction in multicomponent alloy solidification [J]. Acta Materialia, 2011, 59: 6133−6144.

[43] GHOSH A, GHOSH M, KALSAR R. Influence of homogenisation time on evolution of eutectic phases, dispersoid behaviour and crystallographic texture for

Al−Zn−Mg−Cu−Ag alloy [J]. Journal of Alloys and Compounds, 2019, 802: 276−289.
[44] ZOLOTOREVSKII V S, TELESHOV V V. Determining the optimal holding time at solutioning temperature from the structural characteristics of aluminum alloy castings [J]. Metal Science and Heat Treatment, 1970, 12: 594−598.
[45] YANG Z, BANHART J. Natural and artificial ageing in aluminium alloys − The role of excess vacancies [J]. Acta Materialia, 2021, 215: 1−11.
[46] ZOU Yan, WU Xiao-dong, TANG Song-bai, ZHU Qian-qian, SONG Hui, CAO Ling-fei. Co-precipitation of T' and η' phase in Al−Zn−Mg−Cu alloys [J]. Materials Characterization, 2020, 169:1−10.
[47] POGATSCHER S, ANTREKOWITSCH H, LEITNER H, EBNER T, UGGOWITZER P J. Mechanisms controlling the artificial aging of Al−Mg−Si alloys [J]. Acta Materialia, 2011, 59: 3352−3363.
[48] MA Pei-pei, LIU Chun-hui, CHEN Qiu-yu, WANG Qing, ZHAN Li-hua, LI Jian-jun. Natural-ageing-enhanced precipitation near grain boundaries in high-strength aluminum alloy [J]. Journal of Materials Science & Technology, 2020, 46: 107−113.
[49] DING Qing-wei, ZHANG Di, PAN Yan-lin, HOU Sheng-li, ZHUANG Lin-zhong, ZHANG Ji-shan. Strengthening mechanism of age-hardenable Al−xMg−3Zn alloys [J]. Materials Science and Technology, 2019, 35: 1071−1080.
[50] HORNBOGEN E, STARKE E A. Theory assisted design of high strength low alloy aluminum [J]. Acta Metallurgica et Materialia, 1993, 41: 1−16.
[51] LABUSCH R. A statistical theory of solid solution hardening [J]. Physica Status Solidi (b), 1970, 41: 659−669.
[52] SHERCLIFF H R, ASHBY M F. A process model for age hardening of aluminium alloys−I. The model [J]. Acta Metallurgica et Materialia, 1990, 38: 1789−1802.
[53] DIXIT M, MISHRA R S, SANKARAN K K. Structure−property correlations in Al 7050 and Al 7055 high-strength aluminum alloys [J]. Materials Science and Engineering A, 2008, 478: 163−172.

镁含量对铸造低锌含量 Al−xMg−3Zn−1Cu 合金的显微组织与力学性能的影响

雷 川，王渠东，汤华平，刘天文，李仲洋，蒋海燕，王 奎，丁文江

上海交通大学 材料科学与工程学院，
轻合金精密成型国家工程研究中心和金属基复合材料国家重点实验室，上海 200240

摘 要：研究镁含量对铸造低 Zn 含量 Al−xMg−3Zn−1Cu(x=3~5，质量分数，%)合金的显微组织与力学性能的影响。随着 Mg 含量的增加，铸态合金的晶粒因为增强的生长抑制效应而得到细化，当 Mg 含量超过 4%时，η-$Mg(AlZnCu)_2$ 相和 S-Al_2CuMg 相的形成受到抑制，而 T-$Mg_{32}(AlZnCu)_{49}$ 相的形成得到促进。镁含量的增加通过增加共晶相尺寸的方式阻碍合金的固溶动力学，但合金的时效硬化却会因为析出动力学的加快和析出物数量密度的提升而加速。铸态、固溶态和峰时效态合金的屈服强度和抗拉强度均随着 Mg 含量的增加而增加，而合金的伸长率则随着 Mg 含量的增加而降低。峰时效 Al−5Mg−3Zn−1Cu 合金的抗拉强度和伸长率分别超过 500 MPa 和 5%。峰时效合金最主要的强化机制是析出强化，这是通过 T'析出物实现的，且随着镁含量的增加而得到加强。

关键词：镁含量；铸造低 Zn 含量 Al−xMg−3Zn−1Cu 合金；显微组织；时效响应；强化机制

(Edited by Bing YANG)